



A new variational method for selective segmentation of medical images

Wenxiu Zhao^a, Weiwei Wang^{a,*}, Xiangchu Feng^a, Yu Han^b

^a School of Mathematics and Statistics, Xidian University, Xi'an 710071, China

^b School of Mathematics and Statistics, Shenzhen University, Shenzhen 518061, China

ARTICLE INFO

Article history:

Received 19 March 2021

Revised 30 June 2021

Accepted 11 August 2021

Available online 8 September 2021

Keywords:

Selective segmentation

Medical image analysis

Active contour

Level set

ABSTRACT

Selective segmentation aims to separate a subset of target objects or regions of interests in an image. It is widely used in medical image analysis for some specific tasks such as extracting anatomic organs or lesions. However, selective segmentation of medical images is usually challenged by their limited imaging quality. In this paper, we propose a two-phase selective segmentation method. The first phase is a pre-processing step, which aims to reduce influence of noise or cluttered background on segmentation. The second phase performs selective segmentation on the preprocessed image. For the first phase, we propose a new image smoothing model which can effectively reduce noise or intensity inhomogeneity inside objects while retain edges of the original image. Moreover, the proposed model has attractive mathematical and physical properties, in that it has one single optimal solution. For the second phase, we propose a modified Gout's active contour method, which can obtain targeted objects more efficiently and accurately. Our main contribution is the new image smoothing model, which can effectively attenuate complicated background but preserve edges of targeted object. Extensive experiments on real medical images show that, our smoothing model can greatly facilitate the second phase, and our method can significantly improve some existing related methods in terms of either visual assessment or quantitative evaluation.

© 2021 Elsevier B.V. All rights reserved.

1. Introduction

Image segmentation has wide applications in medical image processing, security monitoring, and among others [1–4]. Existing image segmentation methods can be divided into two categories: semantic segmentation [5–8] and selective segmentation [9–14]. Semantic image segmentation aims to divide the image domain into disjoint union of sub-regions, with each sub-region corresponding to a semantic meaningful object. Different from semantic segmentation, the goal of selective segmentation is to separate a subset of objects or regions of interests (ROI) in an image from others. Selective segmentation is widely used in medical image analysis for some specific tasks such as extracting anatomic organs or lesions [15,16]. In this work, we focus on selective segmentation of medical images, which usually have low contrast, inhomogeneous intensity and high level noise, and these adverse factors bring great challenges in selective segmentation.

In the past decades, the variational modeling of selective segmentation has been widely attended and it has good interpreta-

tion than deep learning based models [17–20]. Existing models fall into three categories: edge-based methods, region-based methods, and their hybridization. Edge-based methods encourage an active contour to evolve towards the boundary of ROI. The snake model proposed by Kass et al. [21] was the first edge-based variational model for target segmentation. However, the model is not intrinsic, or the solution depends on parameterization of the contour. To overcome this, Caselles et al. [22] proposed the geodesic activity contour (GAC) model, which uses an image gradient dependent edge stopping function to stop the evolving curve on the desired object boundary. To make the edge detection robust to noise, the image is usually filtered by the isotropic Gaussian filter before computing gradient, but this makes the edge detection inexact. In all, the major challenge that these models meet is that, the evolving curve cannot fit the boundary exactly when the image intensity is inhomogeneous, or the contrast is low, or the image is heavily affected by noise. Gout et al. [23] defined a distance function by using some marker points around the desired boundary, and introduced this distance function into the GAC model. The distance of the points on the desired boundary is small, which helps to attract the evolving curve close to the desired boundary. Moreover, the distance function is independent of image intensity, thus it is robust to image intensity, contrast, and noise. However, Gout's model still suffers from the limitation of GAC.

* Corresponding author.

E-mail addresses: zhaowenxiucn@163.com (W. Zhao), wwwang@mail.xidian.edu.cn (W. Wang), xcfeng@mail.xidian.edu.cn (X. Feng), hany@szu.edu.cn (Y. Han).

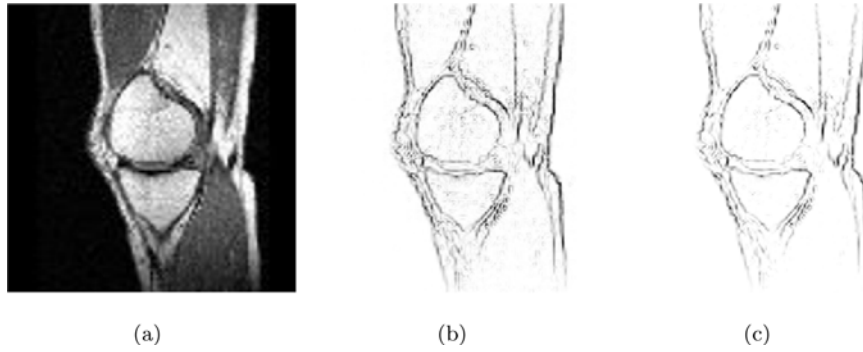


Fig. 1. (a) original noisy image f ; (b) image of $g(|\nabla f|)$; (c) image of $g(|\nabla_{GSC} f|)$.

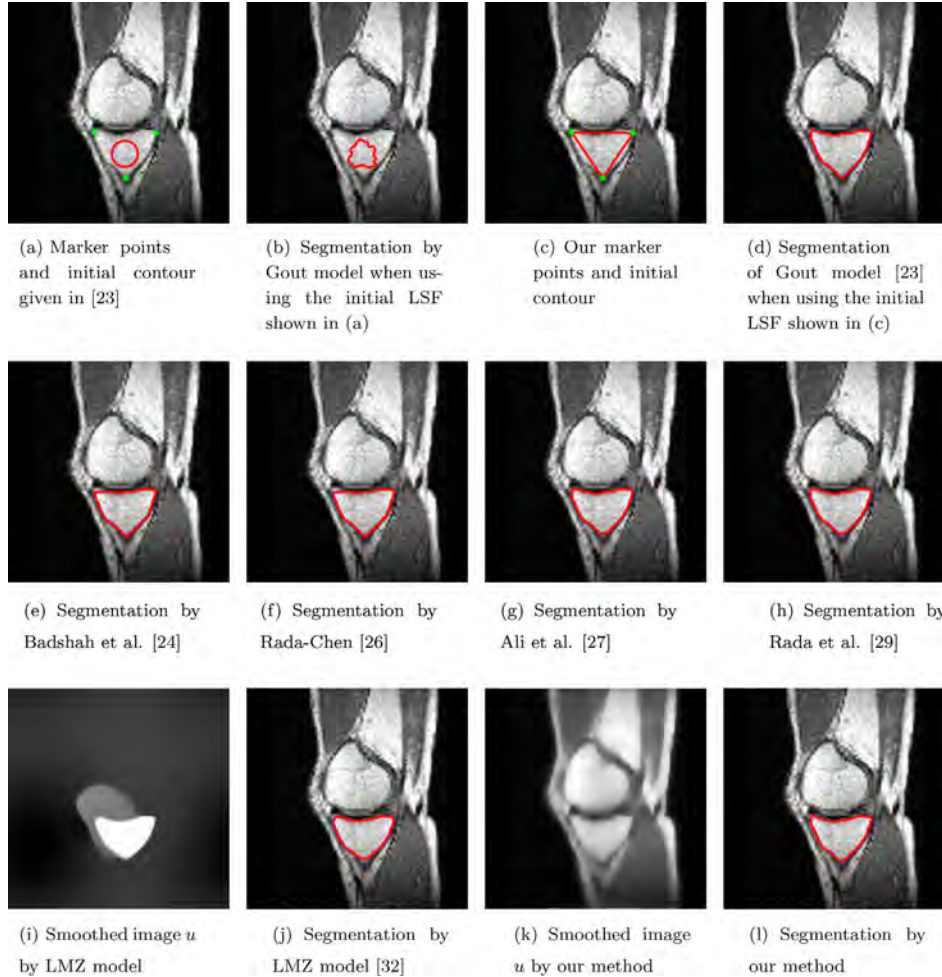


Fig. 2. Segmentation results of a leg image.

To improve Gout's model [23], some models have been proposed by introducing region information for better segmentation accuracy and robustness. Badshah et al. [24] incorporated the intensity fitting terms of Chan-Vese model [25] into the Gout's model. The resulted model performs well in segmenting images with noise or fuzzy boundaries. In [26], Rada et al. added an area fitting term into the model in [24]. In [27], Ali et al. further used the generalized average fitting terms to improve the reliability of the model in [26] for selective segmentation of multi regions. In [28], Rada and Chen proposed a variational model with two level set functions to simultaneously accomplish two tasks: one is global segmentation that captures boundaries of all objects, and the other

is selective segmentation that focuses on a selected object. In [29], Rada et al. proposed a new level-set model to deal with intensity inhomogeneity and presence of noise for selective segmentation. In [30], Roberts et al. proposed a convex selective segmentation model using edge-weighted geodesic distance. A more detailed description of selective segmentation can be found in [31].

All the above selective segmentation models aim to search for the contour of the targeted object. Instead, Liu et al. [32] proposed a two-phase method to locate the region that the target object occupies. First, a smoothed version of the given image is obtained by using their proposed model. The major advantage of this model is that, the distance function and the edge indicating function in

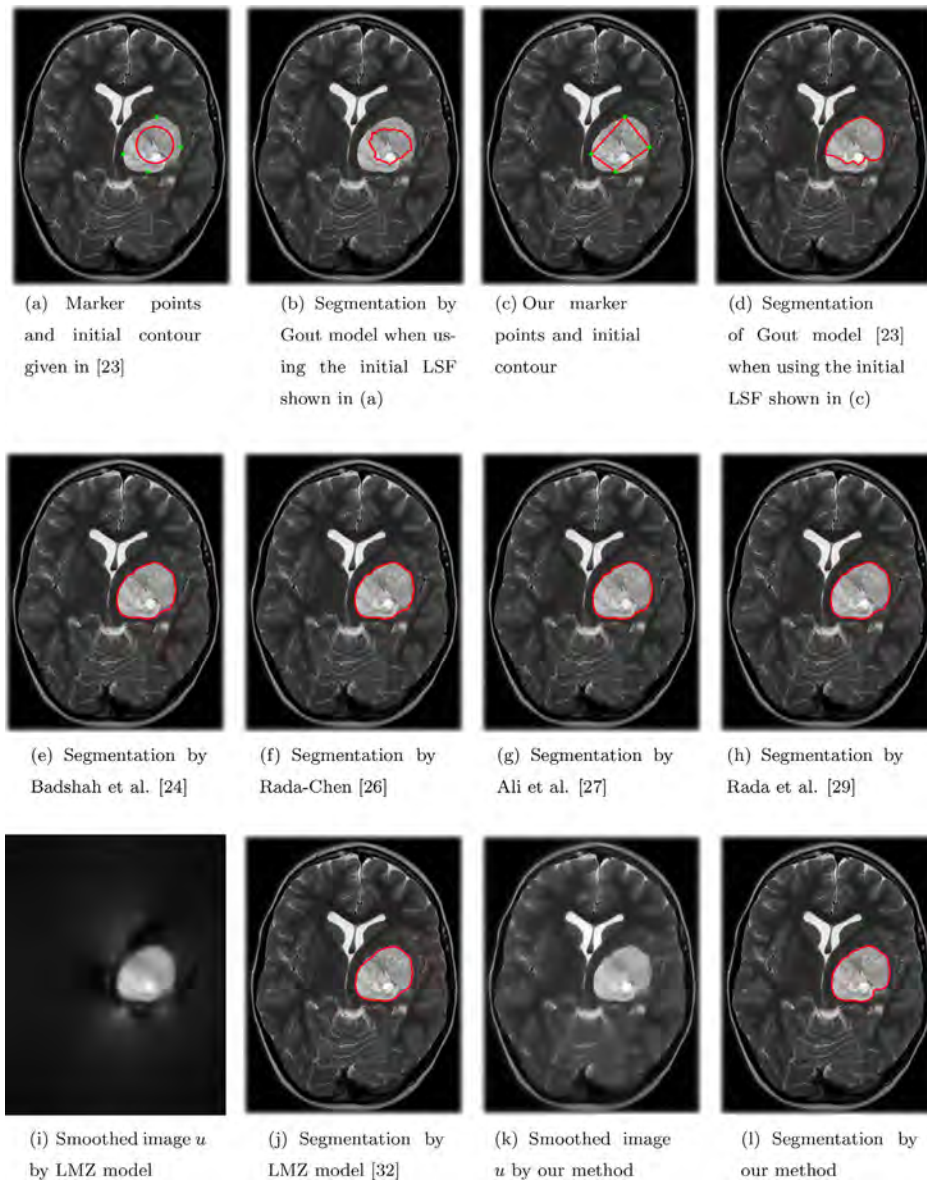


Fig. 3. Segmentation results of a brain tumor.

[26] were used to preserve the target region while other regions are smoothed. This operation greatly facilitates the second phase, in which the target region is located by thresholding the gray level of the smoothed image. However, the optimal threshold is hard to find and the method may produce spurious objects when the image contrast is low and there are multiple objects close to the target object.

In this paper, we propose a new two-phase method for selective segmentation of medical images. Our main contributions can be summarized as follows.

1) Aiming at facilitating medical image segmentation, we present a new variational model, which can effectively attenuate complicated background but preserve edges of targeted object. The proposed energy functional has attractive mathematical properties, thus allows one unique solution in a Hilbert space and the gradient method can be used to find the minimizer. Compared with the smoothing model in [32], our model has several favorite advantages described in Section 3.

2) We modify the Gout's model by using a more stable method to compute image gradients and introducing a scale factor in the

edge stopping function. We also give a new initialization method for the level set function used in solving Gout's model.

3) We give a new two-phase selective image segmentation method. In the first phase, the image is smoothed by using our proposed model. Then in the second phase, the modified Gout's model is used on the smoothed image to detect the target boundary. Extensive experiments on real medical images show that, our smoothing model can greatly facilitate the second phase, and our method can significantly improve two existing related methods in terms of either visual assessment or quantitative evaluation.

2. Related works

In this section, we briefly review some related work, including the model in [23] and the method in [32]. In the following, we call the model in [23] Gout model and the method in [32] LMZ model.

2.1. Gout model [23]

Let $f(x, y)$ be the given image defined on a rectangular domain Ω . Selective segmentation aims to find a contour $\Gamma \subset \Omega$ such that

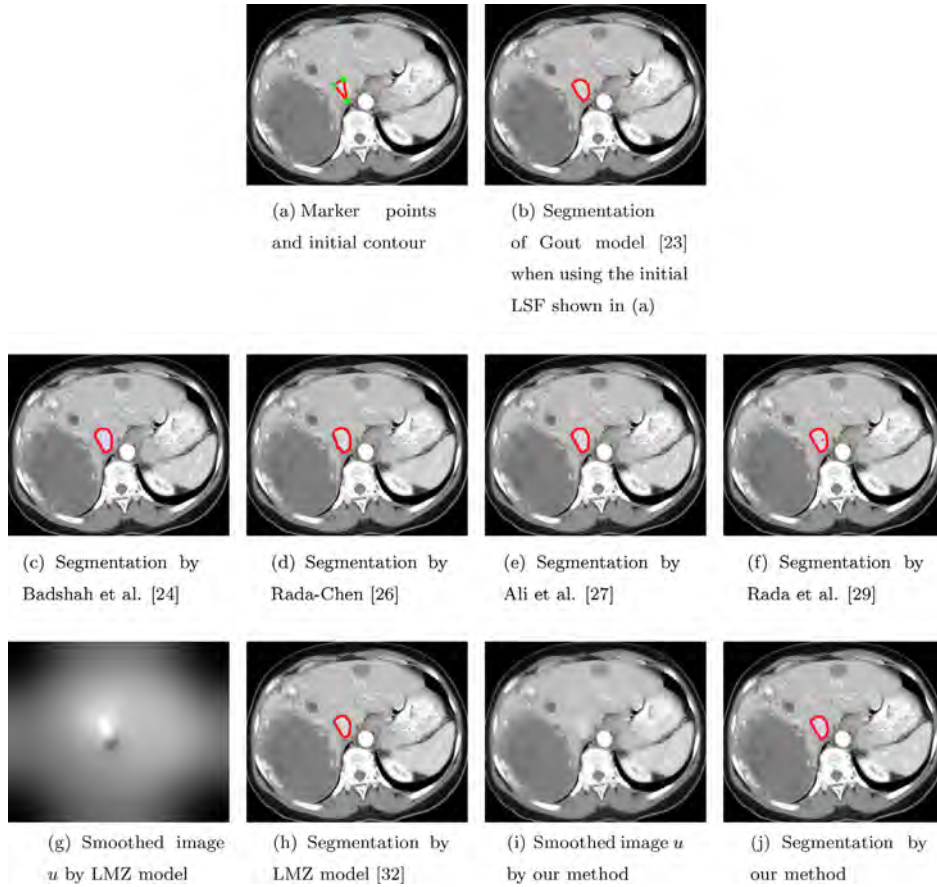


Fig. 4. Segmentation of a small organ from a CT image.

Γ covers the boundary of the object to be detected. The GAC model uses the following image gradient dependent edge stopping function to stop the evolving curve on the desired object boundary

$$g(|\nabla f(x, y)|) = \frac{1}{1 + |\nabla f(x, y)|^2}. \quad (1)$$

However, the evolving curve cannot fit the boundary exactly when the image intensity is inhomogeneous, the contrast is low, or the image is heavily affected by noise. Gout et al. [23] defined a distance function by using some marker points around the desired boundary to facilitate the curve evolution. Let $S = \{(x_i, y_i) \in \Omega, 1 \leq i \leq n\}$ be a set of n marker points around the boundary of the target object. The distance function is defined as follows:

$$d(x, y) = \min_{(x_i, y_i) \in S} |(x, y) - (x_i, y_i)|. \quad (2)$$

Another option is [9]

$$d(x, y) = \prod_{i=1}^n \left(1 - e^{-\frac{(x-x_i)^2}{2\sigma^2}} e^{-\frac{(y-y_i)^2}{2\sigma^2}} \right) \forall (x, y) \in \Omega \quad (3)$$

where $d(x, y)$ is tuned by a parameter σ to allow for adjustment according to the number of points to be fitted. Obviously, the distance function $d(x, y)$ is close to zero near the marker points and close to one wherever far away from the marker points. In order to find the desired contour Γ , Gout et al. minimize the following energy functional:

$$\min_{\Gamma} \int_{\Gamma} d(x, y)g(|\nabla f(x, y)|)ds. \quad (4)$$

Clearly, this model drives the curve Γ stop on the target boundary where both d and g are small. However, it is difficult to segment

targets accurately when the image noise is strong or the target region is cluttered.

2.2. LMZ model [32]

In [32], Liu et al. proposed the following variational model for image smoothing:

$$\min_{u(x, y) \in W^{1,2}(\Omega)} \int_{\Omega} |\nabla u| dx dy + \frac{\alpha}{2} \int_{\Omega} |\nabla u|^2 dx dy + \frac{\beta}{2} \int_{\Omega} w^2 |u - f|^2 dx dy \quad (5)$$

where α, β are nonnegative parameters, $w^2(x, y) = 1 - d(x, y)g(|\nabla f(x, y)|)$ is a weight function to adjust the fidelity term, $d(x, y)$ is defined as that in Eq. (3), and $g(|\nabla f(x, y)|)$ is defined as follows:

$$g(|\nabla f(x, y)|) = \frac{1}{1 + k|\nabla f(x, y)|^2} \quad (6)$$

where $k > 0$ adjusts the strength of gradients. It can be seen that, the first two terms in Eq. (5) are regularity terms, which tends to make u smooth; the third term is the fidelity term and the weight w tends to make the smoothed image u close to the original image at the marker points and image edges. Once u is obtained, then in the second stage, the target of interest is obtained by thresholding u with a proper threshold. This method performs very well by using the optimal threshold. However, it is hard to find, especially when the image contrast is low and there are multiple objects adjacent to the target object.

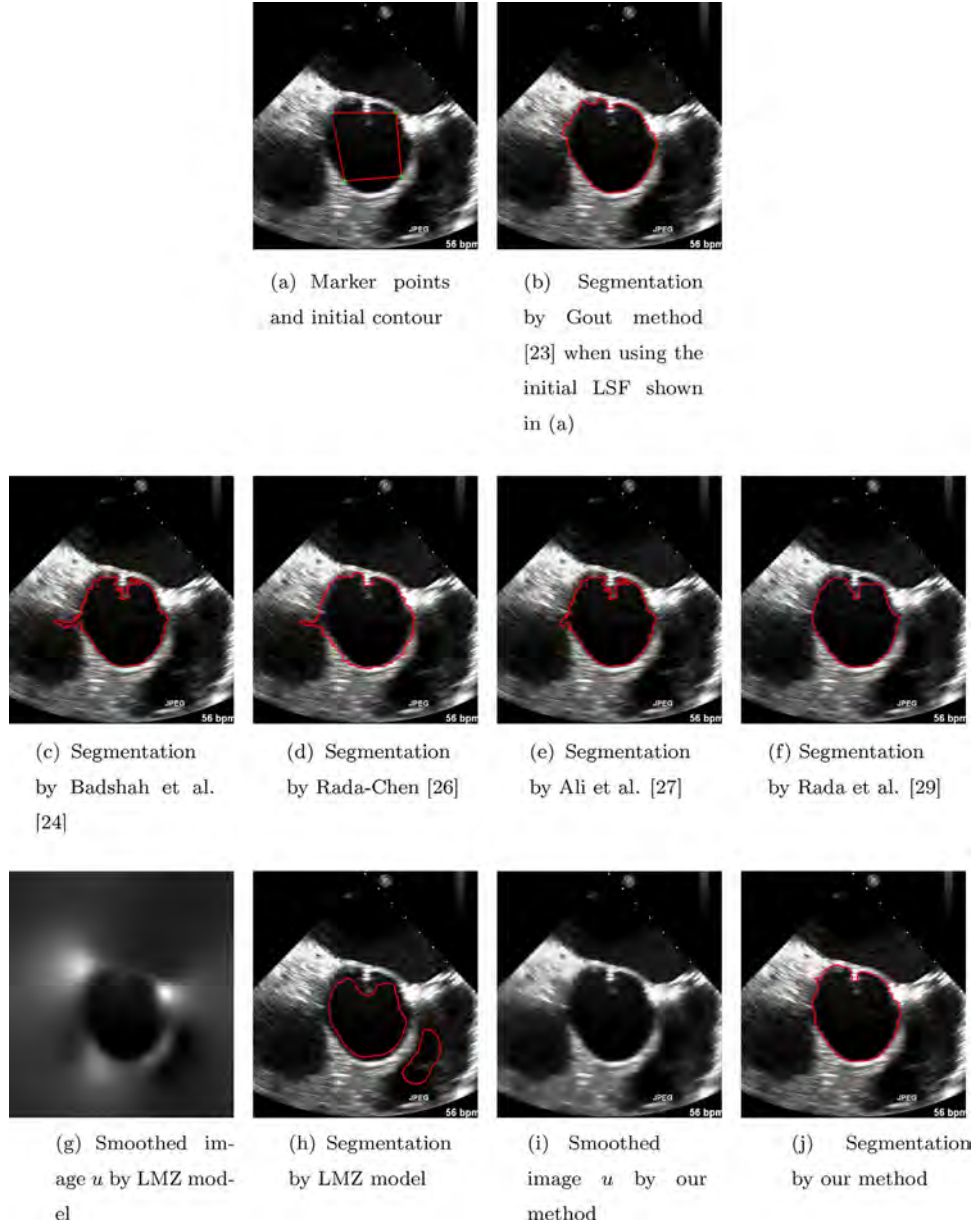


Fig. 5. Segmentation of an ultrasonic image.

3. The proposed method

The major challenge to Gout model is the noise or intensity inhomogeneity, which causes false edge detection. And the major difficulty of LMZ model is the threshold estimation. In this work, we still use Gout’s model to locate the target boundary. However, to tackle the major challenge, we propose a new variational model to smooth the given image in advance. In the following equations, we will drop the variable (x, y) if it is self-explanatory.

3.1. Proposed model

The proposed model is as follows:

$$\min_{u \in W^{1,2}(\Omega)} E(u) := \frac{1}{2} \int_{\Omega} (1 - g(|\nabla_{GSG} f(x, y)|))(u - f)^2(x, y) dx dy + \frac{\alpha}{2} \int_{\Omega} g(|\nabla_{GSG} f(x, y)|) |\nabla u|^2(x, y) dx dy \quad (7)$$

where $\nabla = (\partial/x \ \partial/y)^T$ is the standard gradient operator, ∇_{GSG} is the global sparse gradient (GSG) operator [33], and g is the edge detection function defined in Eq. (6). The first term is the fidelity term and the second one is a regularization term. It is easy to see, in smooth area, $g \approx 1$, the model tends to smooth the image, thus removing noise and small scale details; while on edges, $g \approx 0$, the model tends to make u close to f , thus preserve edges in the smoothed image u .

Three interesting aspects of our model should be noted. First, for the edge detection function g , we use the GSG model [33] to compute the gradient of f because it is more robust to noise than the traditional gradient operator. Fig. 1 shows the images of $g(|\nabla f|)$ and $g(|\nabla_{GSG} f|)$ for a noisy image f . It can be seen that the later one is much more robust to noise. Second, the weight of our fidelity term only depends on image edges so that the image smoothing phase is independent of the marker points. Third, our regularity does not use the total variation (TV) term [32] in Eq. (5). In fact, our regularity can be regarded as a weighted semi-

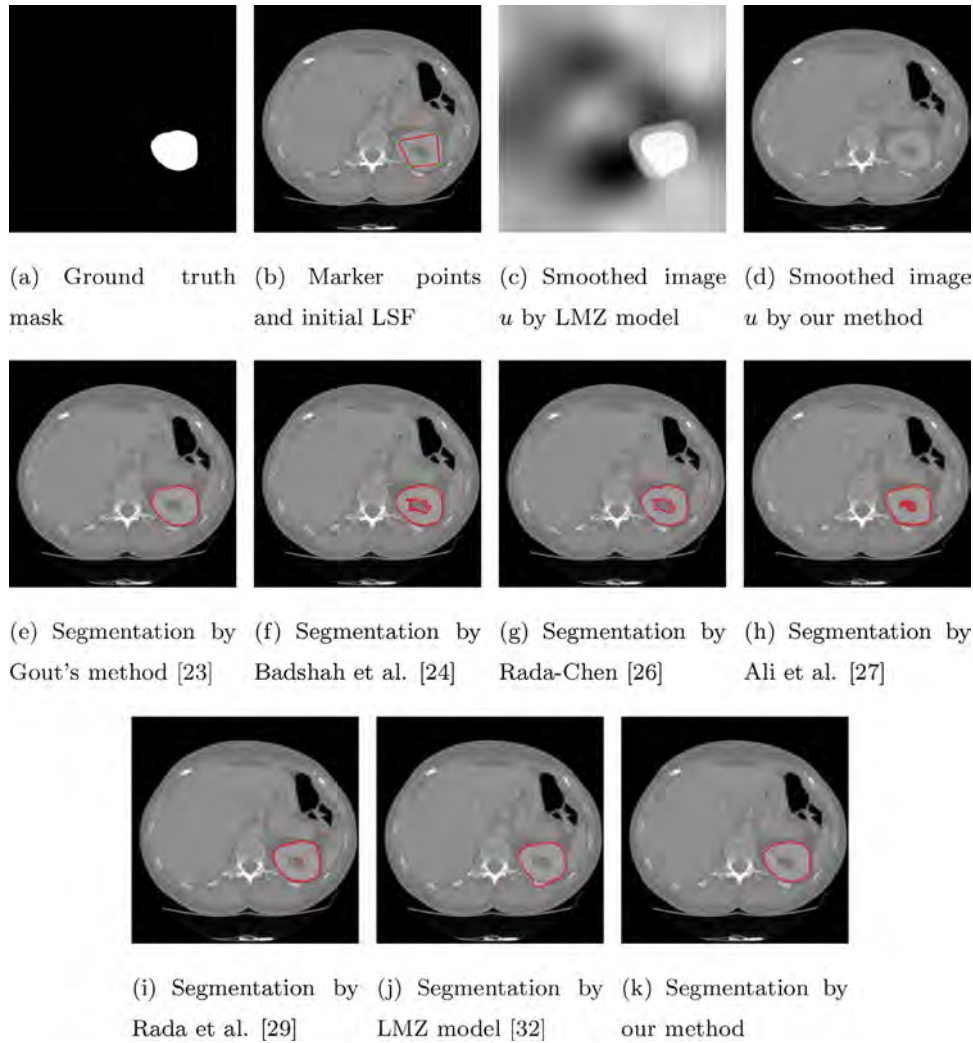


Fig. 6. Segmentation an object with complicated details.

norm of the Sobolev space $W^{1,2}(\Omega)$ [34]. Therefore, our variational problem is well-posed in $W^{1,2}(\Omega)$ and it has one single global solution, which will be analyzed in the following subsection. Moreover, the functional is differentiable, thus allows the gradient descent method.

3.2. Mathematical analysis of proposed model

In theory, it may happen that $|\nabla_{GSG}f|=0$ or $|\nabla_{GSG}f| \rightarrow \infty$. But in computation, we find that $|\nabla_{GSG}f|$ usually has a positive maximum value and a positive minimum value, so does $g(|\nabla_{GSG}f|)$ defined in Eq. (6). We assume $0 < m \leq g(|\nabla_{GSG}f|) \leq M < 1$, then

$$0 < 1 - M \leq 1 - g(|\nabla_{GSG}f|) \leq 1 - m. \tag{8}$$

Having this, we can conclude that our model (7) has one unique solution in $W^{1,2}(\Omega)$.

Proposition 1. Suppose $f \in L^2(\Omega)$. Then the proposed model (7) is strictly convex and there exists a unique minimizer $u^*(x, y) \in W^{1,2}(\Omega)$.

Moreover, the solution satisfies the following extreme principle.

Proposition 2. Suppose $f \in L^2(\Omega)$, the unique minimizer u^* of our model (7) satisfies $\inf_{(x,y) \in \Omega} f(x, y) \leq u^*(x, y) \leq \sup_{(x,y) \in \Omega} f(x, y)$.

Proofs of Proposition 1 and 2 are given in Appendix B.

3.3. Modified active contour model

When the smoothed image u is obtained, we use the following active contour model to locate the target boundary. To leverage the advantages of the level set method [35,36], we rewrite the new model in the level set formulation:

$$\min_{\phi} F(\phi) = \int_{\Omega} g(|\nabla_{GSG}u(x, y)|) |\nabla H(\phi(x, y))| dx dy \tag{9}$$

where H is the Heaviside function, the level set function (LSF) $\phi : \Omega \rightarrow \Re$ is a Lipschitz function, satisfying

$$\begin{cases} \Gamma & = \{(x, y) \in \Omega : \phi(x, y) = 0\} \\ \text{inside}(\Gamma) & = \{(x, y) \in \Omega : \phi(x, y) > 0\} \\ \text{outside}(\Gamma) & = \{(x, y) \in \Omega : \phi(x, y) < 0\} \end{cases}$$

and Γ is the zero level set. Note that our model is different from Gout's model and has some advantages. On one hand, our model uses $g(|\nabla_{GSG}u(x, y)|)$ to detect edge of the target object. This not only makes edge detection robust to noise or complicated background, but also makes computation easy because $g(|\nabla_{GSG}u(x, y)|)$ is computed in the first phase and it is at hand in the second phase. On the other hand, we do not use the distance function, which further makes computation of the second phase simpler. In our method, the marker points is only used to construct the initial active contour.

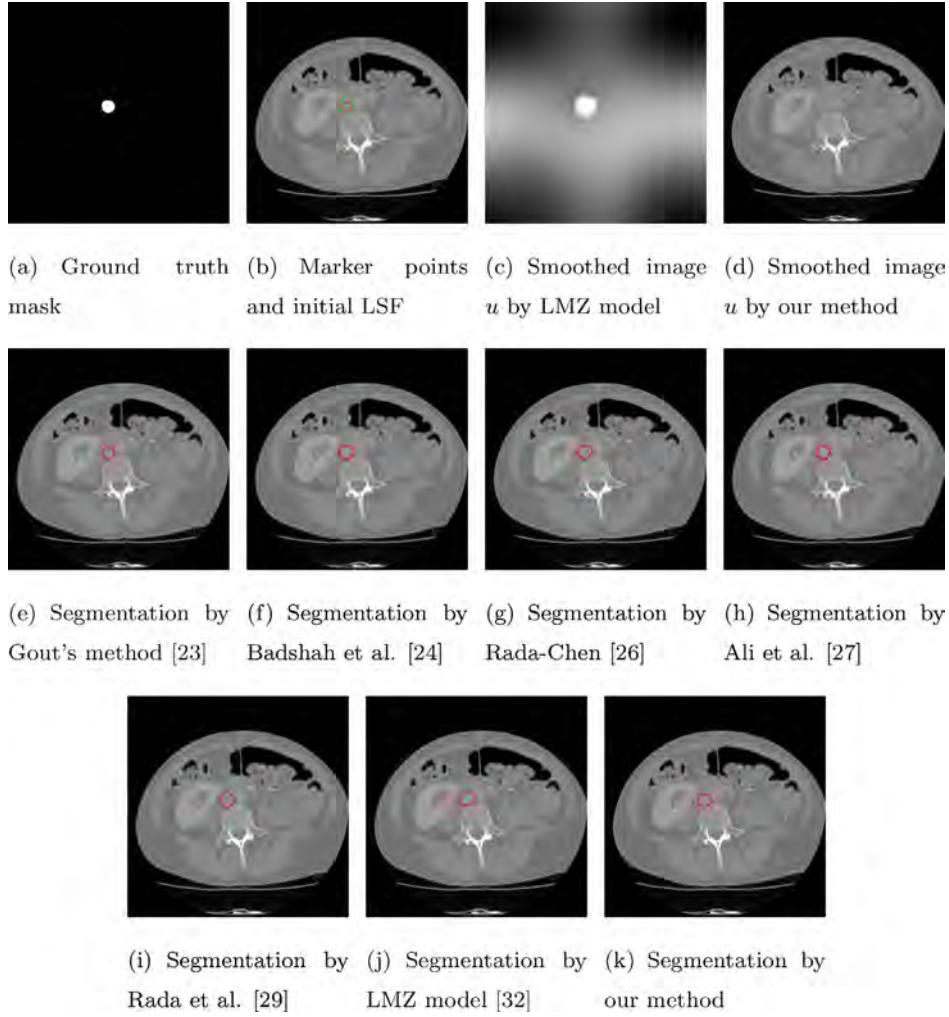


Fig. 7. Segmentation of a small-sized object.

3.4. Numerical algorithm

To solve Eq. (7) for u , we first find the Euler-Lagrange equation as follows:

$$(1 - g(|\nabla_{GSG}f|))(f - u) + \alpha g(|\nabla_{GSG}f|)\Delta u = 0. \quad (10)$$

Then introduce an artificial time instant t and embed the above equation into the following evolution equation:

$$\frac{\partial u}{\partial t} = (1 - g(|\nabla_{GSG}f|))(f - u) + \alpha g(|\nabla_{GSG}f|)\Delta u. \quad (11)$$

For easy computation, we use explicit difference (in t) to discretize the above equation with step-size τ_1 and get the following iteration scheme:

$$u^{t+1} = u^t + \tau_1 [(1 - g(|\nabla_{GSG}f|))(f - u) + \alpha g(|\nabla_{GSG}f|)\Delta u]^t. \quad (12)$$

For better stability, one can also use implicit difference (in t).

In our experiment, to further reduce the influence of noise, we use the intermediate smooth image u^t instead of the original noisy image f for edge detection. The actual evolution equation we used is

$$u^{t+1} = u^t + \tau_1 [(1 - g(|\nabla_{GSG}u^t|))(f - u^t) + \alpha g(|\nabla_{GSG}u^t|)\Delta u^t]. \quad (13)$$

We take the given image f as the initial u , or we set $u^0 = f$. On the boundary of Ω , we use the Neumann boundary condition: $\frac{\partial u}{\partial N} = 0$ on $\partial\Omega$ (N is the outward normal to $\partial\Omega$).

Now we present the solution of model (9) for ϕ . Note that H is not differentiable at the origin, so we use the regularized version of H , denoted by H_ε and is given by Chan and Vese [25], Osher and Fedkiw [35]:

$$H_\varepsilon(\phi) = \frac{1}{2} \left(1 + \frac{2}{\pi} \arctan \left(\frac{\phi}{\varepsilon} \right) \right) \partial\Omega \quad (14)$$

and $\delta_\varepsilon = H'_\varepsilon = \frac{1}{\pi} \frac{\varepsilon}{\varepsilon^2 + \phi^2}$. The energy in Eq. (9) can be written as

$$F_\varepsilon(\phi) = \int_{\Omega} g(|\nabla_{GSG}u(x, y)|) \delta_\varepsilon(\phi) |\nabla\phi(x, y)| dx dy. \quad (15)$$

The associated Euler-Lagrange equation for ϕ is

$$-\delta_\varepsilon(\phi) \operatorname{div} \left(g(|\nabla_{GSG}u|) \frac{\nabla\phi}{|\nabla\phi|} \right) = 0. \quad (16)$$

The corresponding evolution equation is

$$\frac{\partial\phi}{\partial t} = \delta_\varepsilon(\phi) \operatorname{div} \left(g(|\nabla_{GSG}u|) \frac{\nabla\phi}{|\nabla\phi|} \right). \quad (17)$$

We use the following explicit difference scheme to discretize the above equation:

$$\phi^{t+1} = \phi^t + \tau_2 \left[\delta_\varepsilon(\phi) \operatorname{div} \left(g(|\nabla_{GSG}u|) \frac{\nabla\phi}{|\nabla\phi|} \right) \right]^t. \quad (18)$$

For our method, we take the polygon connecting the marker points as the initial contour. Instead of using the signed distance function,

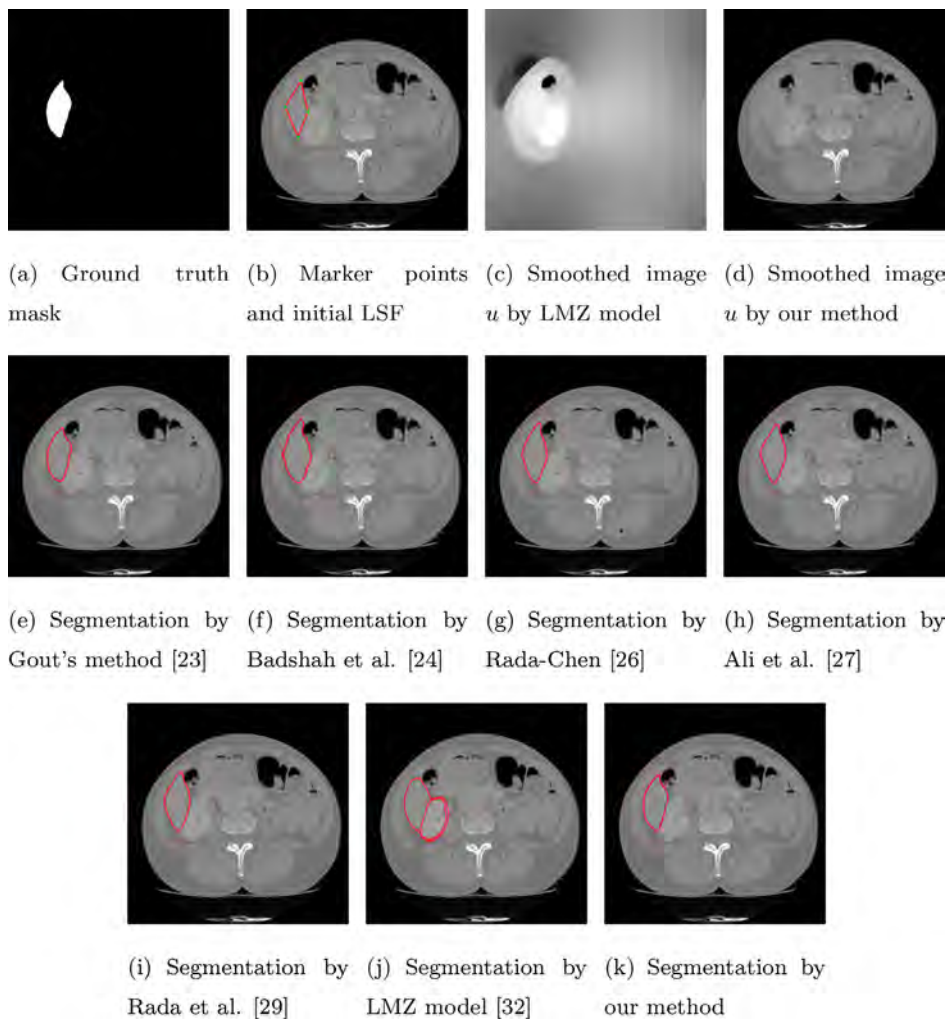


Fig. 8. segmentation of an object occluded with adjacent objects.

we define the initial LSF simply by

$$\phi^0(x, y) = \begin{cases} +c, & \text{if } (x, y) \text{ is inside } P \\ 0, & \text{if } (x, y) \text{ is on } P \\ -c, & \text{if } (x, y) \text{ is outside } P \end{cases}$$

where P denotes the polygon and c is a constant. Such initialization of the LSF is computationally more efficient than the signed distance function, and empirically very effective in our experiments. On the boundary of Ω , we use the Neumann boundary condition: $\frac{\delta_\epsilon(\phi)}{|\nabla\phi|} \frac{\partial\phi}{\partial N} = 0$, N denoting the unit exterior normal to the boundary of Ω .

4. Experimental results

In this section, we present some segmentation results on real medical images to illustrate the performance of the proposed method. We compare our proposed method with some previous models, including Gout model [23], Badshah et al. [24], Rada-Chen [26], Ali et al. [27], Rada et al. [29] and LMZ model [32]. The results of the Ali et al. [27], Rada et al. [29] and LMZ model [32] are obtained by running the codes provided by the authors. The codes of Badshah et al. [24] and Rada-Chen [26] are written by ourselves according to the code of Ali et al. [27]. The results of Gout's method and our method are obtained by using our codes. For all methods, we choose the same set of marker points, marked in the original image by green stars around the boundary of the target. The meth-

ods in [23,24,26,27,29] and our method use the same initial level set. The final located boundary of the target is superimposed on the given image as a red curve. The parameters of our method are manually selected for the presented results. The parameters of all methods are provided in Appendix A, Table A.1.

4.1. Visual assessment and comparison

First, we present the segmentation results of some commonly used medical images for visual comparison with the methods in [23,24,26,27,29,32]. We do not give quantitative comparison because we do not have the ground-truth segmentation. Fig. 2 shows the results of a bone image, which has strong noise. With three marking points, the initial LSF and edge stopping function given in [23], the desired contour cannot be obtained, as shown in Fig. 2(a) and (b). It mainly because the original image is noisy and edge detection is not exact. In addition, different initial contours also affect the segmentation results. However, when using our initialization of the LSF and the edge stopping function with scaled gradients, the segmentation of Gout's method can be significantly improved, as shown in Fig. 2(c) and (d). So, in the followed experiments, we use our initial LSF and the same scaling constant k for Gout's model and our method. For both methods, we also use the same iteration stopping criterion: the difference between two successive LSFs is within a tolerance. The LMZ method first smooths the noisy original image so that the target is highlighted while others

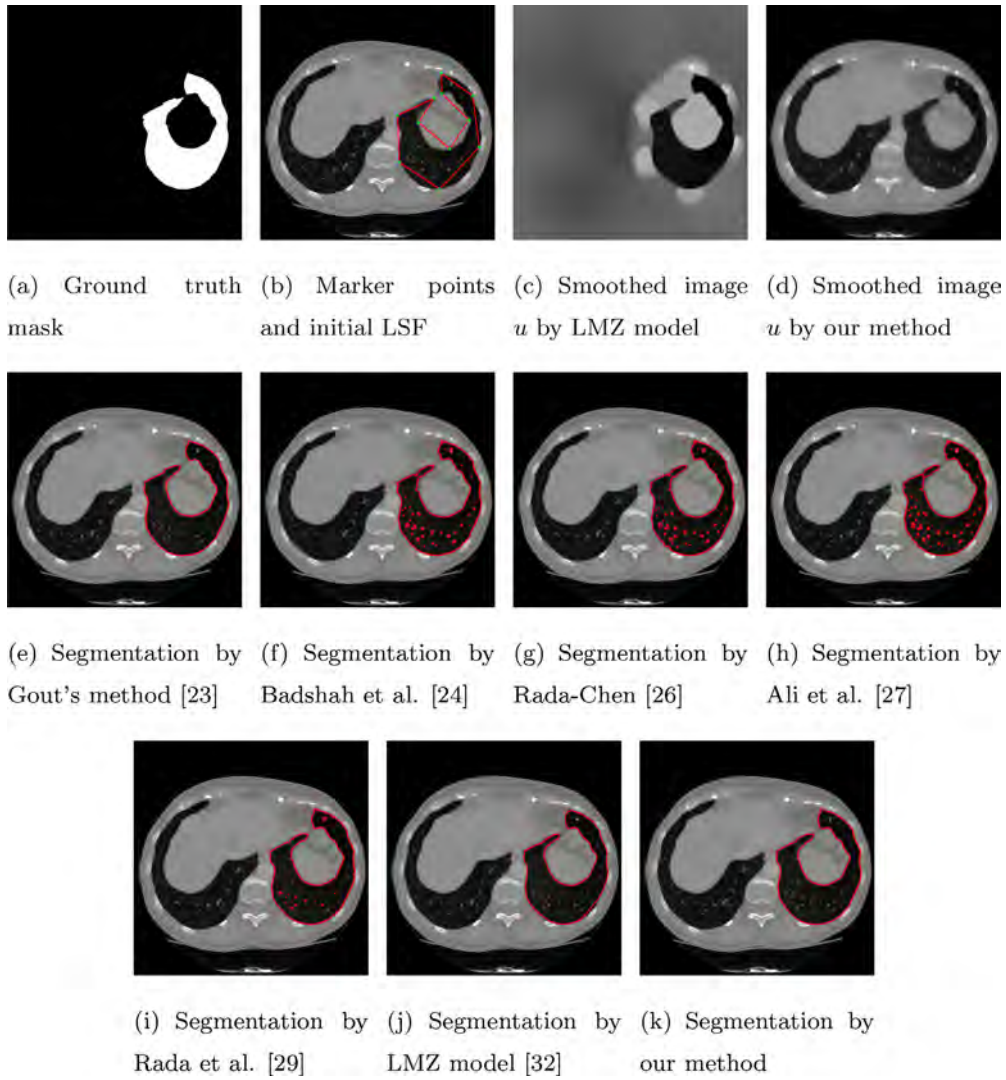


Fig. 9. segmentation of a large object with complicated shape.

are diminished. Then a thresholding operation is performed on the smoothed image to get the final segmentation. Our method also smooths the noisy original image, but with a different purpose. We aim to remove the noise while keep the edges, so the boundaries of all objects will be preserved, and the smooth image can be used for other applications. We apply the modified active contour model (9) to locate the boundary of the target. It can be seen that, the final segmentation perfectly matches the real boundary of the target. This confirms that, our smoothing process greatly facilitate the followed active contour evolution. By using our marker points and initial contour, the methods in [24,26,27,29] obtain segmentation results on par with ours.

Fig. 3 shows segmentation of a tumor from a brain MRI. Since the tumor has complicated details, the Gout model fails by using either their initialization or our initialization. In comparison, it is successfully segmented by using other model and our proposed method. Fig. 4 shows segmentation of a small sized object from a CT image. The noise is strong and the intensity contrast is extremely low, all methods can successfully detect the object. Fig. 5 shows segmentation of an object from an ultrasonic image. Obviously, the image has strong noise and the boundary of the target is not regular. Four marker points are chosen. By using our initial LSF and scaling constant k , the Gout model, Rada et al. and our method performs very well. However, LMZ model fail in this case. It is mainly because the target and the nearby objects have

similar intensity, thus it is hard to find the just right threshold for exact segmentation. The segmentations obtained by the methods in [24,26,27] are not exact due to the fuzzy edges of the target region.

4.2. Quantitative assessment and comparison

In this section, we evaluate our proposed method quantitatively and compare it with Gout model [23], Badshah et al.[24], Rada-Chen[26], Ali et al. [27], Rada et al. [29], LMZ model [32]. All methods are tested on some abdominal CT images selected from the 3D-IRCADb-01 database.¹ The dataset provides the ground truth masks of the target organs so that we can evaluate the results by the following commonly used metrics, including Dice coefficient, the Jaccard index, precision and recall [37,38]. They are defined as follows:

$$Dice(R_{seg}, R_{gt}) = \frac{2|R_{seg} \cap R_{gt}|}{|R_{seg}| + |R_{gt}|}$$

$$Jaccard(R_{seg}, R_{gt}) = \frac{|R_{seg} \cap R_{gt}|}{|R_{seg} \cup R_{gt}|}$$

$$Precision = \frac{|R_{seg} \cap R_{gt}|}{|R_{seg}|}$$

¹ The dataset is available from <http://ircad.fr/research/3d-ircadb-01>.

Table 1
Quantitative comparisons of our proposed method and other methods.

Images	Method	Dice	Jaccard	Precision	Recall
Fig. 6	Gout model [23]	0.9841	0.9686	0.9969	0.9716
	Badshah et al. [24]	0.9064	0.8288	1	0.8288
	Rada-Chen [26]	0.9218	0.8550	0.9980	0.8565
	Ali et al. [27]	0.9318	0.8723	0.9809	0.8874
	Rada et al. [29]	0.9743	0.9499	0.9767	0.9720
	LMZ model [32]	0.9540	0.9120	0.9462	0.9619
	Our method	0.9864	0.9731	0.9970	0.9760
Fig. 7	Gout model [23]	0.8964	0.8122	1	0.8122
	Badshah et al. [24]	0.9071	0.8299	0.8850	0.9303
	Rada-Chen [26]	0.9282	0.8660	0.9191	0.9374
	Ali et al. [27]	0.9247	0.8599	0.9518	0.8990
	Rada et al. [29]	0.9406	0.8879	0.9245	0.9573
	LMZ model [32]	0.8545	0.7460	0.7985	0.9189
	Our method	0.9634	0.9294	0.9925	0.9360
Fig. 8	Gout model [23]	0.9488	0.9025	0.9808	0.9187
	Badshah et al. [24]	0.9119	0.8381	0.8557	0.9760
	Rada-Chen [26]	0.9186	0.8495	0.9235	0.9138
	Ali et al. [27]	0.9221	0.8555	0.9285	0.9158
	Rada et al. [29]	0.9265	0.8631	0.9037	0.9506
	LMZ model [32]	0.8843	0.7926	0.8218	0.9572
	Our method	0.9615	0.9258	0.9707	0.9524
Fig. 9	Gout model [23]	0.9710	0.9436	0.9996	0.9439
	Badshah et al. [24]	0.9274	0.8646	1	0.8646
	Rada-Chen [26]	0.9318	0.8724	1	0.8724
	Ali et al. [27]	0.9334	0.8752	1	0.8752
	Rada et al. [29]	0.9614	0.9256	0.9999	0.9257
	LMZ model [32]	0.9488	0.9026	0.9997	0.9028
	Our method	0.9735	0.9484	0.9997	0.9486

$$\text{Recall} = \frac{|R_{\text{seg}} \cap R_{\text{gt}}|}{|R_{\text{gt}}|}$$

where $|R_{\text{seg}}|$ and $|R_{\text{gt}}|$ denotes the areas of the segmented region and the ground truth region, respectively, $|R_{\text{seg}} \cap R_{\text{gt}}|$ denotes the area of their intersection, $|R_{\text{seg}} \cup R_{\text{gt}}|$ denotes the area of their union. For all of these metrics, larger values indicate better segmentation performance.

Figs. 6–9 show the segmentation results of four different organs: left kidney, venous system, liver, and left lung, respectively. The common challenges of these test images are, all have strong noise and low contrast. Each image has its particular challenge. For example, the target in Fig. 6 has complicated details, the target in Fig. 7 is relatively small, the target in Fig. 8 is occluded with adjacent objects and they have similar intensity, and the target in Fig. 9 has very complicated boundary. With the same initial LSFs and same scaling constants k , the skilled Gout model performs almost as well as ours on these test images. For the image shown in Figs. 6 and 8, the LMZ method detected both the target object and its adjacent object whereas our method detects the target object correctly. For the image shown in Figs. 6 and 9, due to intensity heterogeneity inside the target regions, the boundary detected respectively by Badshah et al. [24], Rada-Chen [26], Ali et al. [27] and Rada et al. [29] contains undesired small fragments, causing over segmentation of the target regions. Table 1 presents the objective metrics, with the best ones in bold. The metrics “Dice”, “Jaccard” of our method are consistently higher than those of other methods. Although the baseline methods obtain higher values of “Precision” and “Recall” on the test images shown in Figs. 6 and 9, the boundaries detected by our method are more accurate.

5. Conclusion

Selective segmentation that extract objects of interest from an image are important and challenging, which is widely used in medical image analysis for some specific tasks such as extracting anatomic organs or lesions. In this paper, we propose a new two-phase method for selective segmentation. In the first phase, we

present a new variational model for image smoothing, which can well preserve the edges and filter out noise and small scale details. Then in the second phase, we use modified Gout’s model to detect the target boundary. We performed extensive segmentation experiments on real medical images, which covers various challenges: strong noise, low contrast, objects with complicated details, small sized objects, objects with complicated boundary, and occluded objects. Experimental results show that our smoothing process can greatly remove some adverse factors in medical images, and our method can significantly outperform the related state-of-the-art selective segmentation methods.

Declaration of Competing Interest

The authors state that there are no conflicts of interest about the publication of this paper.

CRediT authorship contribution statement

Wenxiu Zhao: Methodology, Investigation, Validation, Visualization, Software, Writing – original draft. **Weimei Wang:** Conceptualization, Methodology, Formal analysis, Supervision, Writing – review & editing. **Xiangchu Feng:** Conceptualization, Methodology, Writing – review & editing. **Yu Han:** Software, Validation, Visualization, Writing – review & editing.

Acknowledgments

The work was supported by the National Natural Science Foundation of China (Grant Nos.61972264, 61772389, 62072312), Natural Science Foundation of Guangdong Province (2019A1515010894) and Natural Science Foundation of Shenzhen (20200807165235002). The authors would like to thank the editors and the anonymous reviewers for their constructive comments and suggestions. They would also like to thank Chunxiao Liu from Hangzhou Normal University, Haider Ali from University of Peshawar and Lavdie Rada from Bahcesehir University for providing their codes and some test images.

Appendix A

Table A.1
Parameter settings for the results shown.

Images	Parameters
Fig. 2	$(\sigma, \Delta t, \varepsilon, k) = (5, 10, 10, 10^3)$ [23] $(\mu, \lambda_1, \lambda_2, \sigma, \Delta t) = (mn/10^3, 0.1, 0.1, 5, 1)$ [24] $(\mu, \lambda_1, \lambda_2, v, \alpha, \Delta t, k, \beta, \varepsilon, h) = (mn/(3 \times 10^3), 0.1, 0.1, 10^{-2}, 10^{-2}, 1, 10^2, 10^{-6}, 1, 1)$ [26] $(\mu, \lambda_1, \lambda_2, v, k, \alpha, \Delta t, \gamma, \varepsilon, h) = (mn/10, 1, 1, 0.1, 10^3, 10^{-2}, 1, 10^{-6}, 1, 1)$ [27] $(\mu, \lambda_1, \lambda_2, v, k, \alpha, \Delta t, \theta, \beta, \varepsilon, h) = (mn/3 \times 10^3), 1, 1, 0.1, 10^3, 10^{-2}, 1, 1, 10^{-6}, 1, 1)$ [29] $(\alpha, \beta, \mu, \lambda, \sigma, k) = (1, 2, 15, 10, 15, 1)$ [32] $(\alpha, \tau_1, k, \varepsilon, \tau_2) = (20, 10^{-2}, 10^3, 10, 10)$ our model
Fig. 3	$(\sigma, \Delta t, \varepsilon, k) = (10, 10, 10, 0.1)$ [23] $(\mu, \lambda_1, \lambda_2, \sigma, \Delta t) = (mn/10^3, 0.1, 0.1, 10, 1)$ [24] $(\mu, \lambda_1, \lambda_2, v, \alpha, \Delta t, k, \beta, \varepsilon, h) = (mn/(3 \times 10^3), 0.1, 0.1, 10^{-2}, 10^{-2}, 1, 1, 10^{-6}, 1, 1)$ [26] $(\mu, \lambda_1, \lambda_2, v, k, \alpha, \Delta t, \gamma, \varepsilon, h) = (mn/10, 1, 1, 0.1, 1, 10^{-2}, 1, 10^{-6}, 1, 1)$ [27] $(\mu, \lambda_1, \lambda_2, v, k, \alpha, \Delta t, \theta, \beta, \varepsilon, h) = (mn/(3 \times 10^3), 0.1, 0.1, 10^{-3}, 1, 10^{-2}, 1, 1, 10^{-6}, 1, 1)$ [29] $(\alpha, \beta, \mu, \lambda, \sigma, k) = (1, 10, 15, 10, 15, 1)$ [32] $(\alpha, \tau_1, k, \varepsilon, \tau_2) = (25, 10^{-2}, 0.1, 10, 10)$ our model
Fig. 4	$(\sigma, \Delta t, \varepsilon, k) = (5, 1, 1, 0.1)$ [23] $(\mu, \lambda_1, \lambda_2, \sigma, \Delta t) = (mn/10^3, 10^{-4}, 10^{-4}, 5, 1)$ [24] $(\mu, \lambda_1, \lambda_2, v, \alpha, \Delta t, k, \beta, \varepsilon, h) = (mn/(3 \times 10^3), 10^{-4}, 10^{-4}, 10^{-2}, 0.1, 1, 1, 10^{-6}, 1, 1)$ [26] $(\mu, \lambda_1, \lambda_2, v, k, \alpha, \Delta t, \gamma, \varepsilon, h) = (mn/10, 10^{-4}, 10^{-4}, 0.1, 0.1, 10^{-2}, 1, 10^{-6}, 1, 1)$ [27] $(\mu, \lambda_1, \lambda_2, v, k, \alpha, \Delta t, \theta, \beta, \varepsilon, h) = (mn/(3 \times 10^3), 10^{-3}, 10^{-3}, 10^{-3}, 1, 10^{-2}, 1, 1, 10^{-6}, 1, 1)$ [29] $(\alpha, \beta, \mu, \lambda, \sigma, k) = (1, 10, 15, 10, 5, 10^{-2})$ [32] $(\alpha, \tau_1, k, \varepsilon, \tau_2) = (15, 10^{-2}, 0.1, 1, 1)$ our model
Fig. 5	$(\sigma, \Delta t, \varepsilon, k) = (15, 10, 10, 0.1)$ [23] $(\mu, \lambda_1, \lambda_2, \sigma, \Delta t) = (mn/10^3, 0.1, 0.1, 15, 1)$ [24] $(\mu, \lambda_1, \lambda_2, v, \alpha, \Delta t, k, \beta, \varepsilon, h) = (mn/(3 \times 10^3), 0.1, 0.1, 10^{-2}, 10^{-2}, 0.1, 0.1, 10^{-6}, 1, 1)$ [26] $(\mu, \lambda_1, \lambda_2, v, k, \alpha, \Delta t, \gamma, \varepsilon, h) = (mn/10, 1, 1, 1, 10^5, 10^{-2}, 1, 10^{-6}, 1, 1)$ [27] $(\mu, \lambda_1, \lambda_2, v, k, \alpha, \Delta t, \theta, \beta, \varepsilon, h) = (mn/(3 \times 10^3), 0.1, 0.1, 10^{-3}, 0.1, 10^{-2}, 0.1, 1, 10^{-6}, 1, 1)$ [29] $(\alpha, \beta, \mu, \lambda, \sigma, k) = (30, 20, 15, 20, 15, 0.1)$ [32] $(\alpha, \tau_1, k, \varepsilon, \tau_2) = (15, 10^{-2}, 0.1, 1, 1)$ our model
Fig. 6	$(\sigma, \Delta t, \varepsilon, k) = (5, 10, 10, 10^5)$ [23] $(\mu, \lambda_1, \lambda_2, \sigma, \Delta t) = (mn/(3 \times 10^3), 0.1, 0.1, 5, 0.1)$ [24] $(\mu, \lambda_1, \lambda_2, v, \alpha, \Delta t, k, \beta, \varepsilon, h) = (mn/(3 \times 10^3), 1, 1, 1, 10^{-2}, 1, 1, 10^{-6}, 1, 1)$ [26] $(\mu, \lambda_1, \lambda_2, v, k, \alpha, \Delta t, \gamma, \varepsilon, h) = (mn/10, 1, 1, 0.1, 10^5, 10^{-2}, 1, 10^{-6}, 1, 1)$ [27] $(\mu, \lambda_1, \lambda_2, v, k, \alpha, \Delta t, \theta, \beta, \varepsilon, h) = (mn/(3 \times 10^3), 0.1, 0.1, 1, 1, 10^{-2}, 1, 1, 10^{-6}, 1, 1)$ [29] $(\alpha, \beta, \mu, \lambda, \sigma, k) = (1, 20, 10, 10, 10, 1)$ [32] $(\alpha, \tau_1, k, \varepsilon, \tau_2) = (25, 0.01, 10^5, 10, 10)$ our model
Fig. 7	$(\sigma, \Delta t, \varepsilon, k) = (10, 10, 10, 10^5)$ [23] $(\mu, \lambda_1, \lambda_2, \sigma, \Delta t) = (mn/(3 \times 10^3), 0.1, 0.1, 5, 0.1)$ [24] $(\mu, \lambda_1, \lambda_2, v, \alpha, \Delta t, k, \beta, \varepsilon, h) = (mn/(3 \times 10^3), 1, 1, 1, 10^{-2}, 0.1, 1, 10^{-6}, 1, 1)$ [26] $(\mu, \lambda_1, \lambda_2, v, k, \alpha, \Delta t, \gamma, \varepsilon, h) = (mn/10, 1, 1, 0.1, 10^6, 10^{-2}, 1, 10^{-6}, 1, 1)$ [27] $(\mu, \lambda_1, \lambda_2, v, k, \alpha, \Delta t, \theta, \beta, \varepsilon, h) = (mn/(3 \times 10^3), 0.1, 0.1, 0.1, 1, 10^{-2}, 1, 1, 10^{-6}, 1, 1)$ [29] $(\alpha, \beta, \mu, \lambda, \sigma, k) = (1, 10, 15, 10, 5, 1)$ [32] $(\alpha, \tau_1, k, \varepsilon, \tau_2) = (25, 10^{-2}, 10^6, 1, 10)$ our model
Fig. 8	$(\sigma, \Delta t, \varepsilon, k) = (15, 10, 10, 10^6)$ [23] $(\mu, \lambda_1, \lambda_2, \sigma, \Delta t) = (mn/(3 \times 10^3), 0.1, 0.1, 5, 0.1)$ [24] $(\mu, \lambda_1, \lambda_2, v, \alpha, \Delta t, k, \beta, \varepsilon, h) = (mn/(3 \times 10^3), 1, 1, 1, 10^{-2}, 0.1, 1, 10^{-6}, 1, 1)$ [26] $(\mu, \lambda_1, \lambda_2, v, k, \alpha, \Delta t, \gamma, \varepsilon, h) = (mn/10, 1, 1, 0.1, 10^6, 10^{-2}, 1, 10^{-6}, 1, 1)$ [27] $(\mu, \lambda_1, \lambda_2, v, k, \alpha, \Delta t, \theta, \beta, \varepsilon, h) = (mn/(3 \times 10^3), 0.1, 0.1, 0.1, 1, 10^{-2}, 1, 1, 10^{-6}, 1, 1)$ [29] $(\alpha, \beta, \mu, \lambda, \sigma, k) = (1, 20, 30, 1, 20, 1)$ [32] $(\alpha, \tau_1, k, \varepsilon, \tau_2) = (25, 10^{-2}, 10^6, 10, 10)$ our model
Fig. 9	$(\sigma, \Delta t, \varepsilon, k) = (15, 10, 10, 10^4)$ [23] $(\mu, \lambda_1, \lambda_2, \sigma, \Delta t) = (mn/(3 \times 10^3), 1, 1, 15, 1)$ [24] $(\mu, \lambda_1, \lambda_2, v, \alpha, \Delta t, k, \beta, \varepsilon, h) = (mn/(3 \times 10^3), 1, 1, 0.1, 10^{-2}, 1, 1, 10^{-6}, 1, 1)$ [26] $(\mu, \lambda_1, \lambda_2, v, k, \alpha, \Delta t, \gamma, \varepsilon, h) = (mn/10, 1, 1, 0.1, 1, 10^{-2}, 10, 10^{-6}, 1, 1)$ [27] $(\mu, \lambda_1, \lambda_2, v, k, \alpha, \Delta t, \theta, \beta, \varepsilon, h) = (mn/(3 \times 10^3), 1, 1, 1, 1, 10^{-2}, 10, 1, 10^{-6}, 1, 1)$ [29] $(\alpha, \beta, \mu, \lambda, \sigma, k) = (1, 5, 40, 10, 15, 1)$ [32] $(\alpha, \tau_1, k, \varepsilon, \tau_2) = (25, 10^{-2}, 10^4, 10, 10)$ our model

Appendix B

Proof of Proposition 1. First, we note that

$$0 \leq \inf_{u \in W^{1,2}(\Omega)} E(u) \leq E(0) \leq \frac{1-m}{2} \int_{\Omega} |f|^2 dx dy < +\infty, \quad (A.1)$$

Thus $\inf_{u \in W^{1,2}(\Omega)} E(u)$ must exist. It is obvious that

$$\|\nabla u\|_{L^2(\Omega)} \leq \sqrt{\frac{2}{\alpha M}} E(u) \quad (A.2)$$

and

$$\|u\|_{L^2(\Omega)} \leq \|u - f\|_{L^2(\Omega)} + \|f\|_{L^2(\Omega)}, \quad (A.3)$$

Meanwhile,

$$0 \leq \frac{1-M}{2} \int_{\Omega} |u - f|^2 dx dy \leq \frac{1}{2} \int_{\Omega} (1 - g(|\nabla_{GSG} f|)) |u - f|^2 dx dy \leq E(u). \quad (A.4)$$

From which we obtain

$$\|u - f\|_{L^2(\Omega)} \leq \sqrt{\frac{2}{1-M}} E(u). \quad (A.5)$$

Combining (A.2), (A.3), and (A.5), we have

$$\begin{aligned} \|u\|_{W^{1,2}(\Omega)} &\leq \|u\|_{L^2(\Omega)} + \|\nabla u\|_{L^2(\Omega)} \\ &\leq \left(\sqrt{\frac{2}{\alpha M}} + \sqrt{\frac{2}{1-M}}\right)\sqrt{E(u)} + \|f\|_{L^2(\Omega)}, \end{aligned} \tag{A.6}$$

This indicates the coerciveness of $E(u)$.

In addition, $W^{1,2}(\Omega)$ is a reflective Banach space, and $E(u)$ is strictly convex, lower semicontinuous (l.s.c.) and coercive. We conclude that there exists one unique minimizer $u^*(x, y)$ of $E(u)$ in $W^{1,2}(\Omega)$ [34,39].

Proof of Proposition 2. Let $w(x, y) = 1 - g(|\nabla_{GSG} f(x, y)|)$, we have $0 < 1 - M \leq w(x, y) \leq 1 - m, \forall (x, y) \in \Omega$. Denote $a = \inf_{(x,y) \in \Omega} f(x, y)$ and $b = \sup_{(x,y) \in \Omega} f(x, y)$.

First we note that, for any fixed point $(x, y) \in \Omega$, we have $F(s) = w(x, y)|s - f(x, y)|^2$ is decreasing over the interval $(0, f)$ and increasing over $(f, +\infty)$. Therefore, if $c \geq f$, we have

$$w|\min(s, c) - f|^2 \leq w|s - f|^2, \forall s \in R.$$

Let $c = b, s = u^*(x, y)$, we have

$$w(x, y)|\min(u^*(x, y), b) - f(x, y)|^2 \leq w(x, y)|u^*(x, y) - f(x, y)|^2, \tag{A.7}$$

for any fixed point $(x, y) \in \Omega$. Therefore,

$$\begin{aligned} \int_{\Omega} w(x, y)|\min(u^*(x, y), b) - f(x, y)|^2 dx dy \\ \leq \int_{\Omega} w(x, y)|u^*(x, y) - f(x, y)|^2 dx dy \end{aligned} \tag{A.8}$$

In the same way we can prove that

$$\begin{aligned} \int_{\Omega} w(x, y)|\max(u^*(x, y), a) - f(x, y)|^2 dx dy \\ \leq \int_{\Omega} w(x, y)|u^*(x, y) - f(x, y)|^2 dx dy \end{aligned} \tag{A.9}$$

On the other hand, from Proposition 15 in [40], both $\min(u^*, b)(x, y)$ and $\max(u^*, a)(x, y)$ fall in $W^{1,2}(\Omega)$ and

$$|\nabla(\min(u^*, b))| \leq |\nabla u^*|, |\nabla(\max(u^*, a))| \leq |\nabla u^*| \tag{A.10}$$

Combing (A.8), (A.9), and (A.10), we have $E(\min(u^*, b)) \leq E(u^*)$, $E(\max(u^*, a)) \leq E(u^*)$. By using the uniqueness of the minimizer, we can conclude $a \leq u^* \leq b$.

References

- [1] I. Oksuz, A. Mukhopadhyay, R. Dharmakumar, et al., Unsupervised myocardial segmentation for cardiac BOLD, *IEEE Trans. Med. Imaging* 36 (11) (2017) 2228–2238.
- [2] A. Makropoulos, I.S. Gousias, C. Ledig, et al., Automatic whole brain MRI segmentation of the developing neonatal brain, *IEEE Trans. Med. Imaging* 33 (9) (2014) 1818–1831.
- [3] A.A. Farag, R.M. Mohamed, A. El-Baz, A unified framework for map estimation in remote sensing image segmentation, *IEEE Trans. Geosci. Remote Sens.* 43 (7) (2005) 1617–1634.
- [4] D. Jolly M-P, S. Lakshmanan, A.K. Jain, Vehicle segmentation and classification using deformable templates, *IEEE Trans. Pattern Anal. Mach. Intell.* 18 (3) (1996) 293–308.
- [5] M. Seyedhosseini, T. Tasdizen, Semantic image segmentation with contextual hierarchical models, *IEEE Trans. Pattern Anal. Mach. Intell.* 38 (5) (2015) 951–964.
- [6] T. Wu, X. Gu, Y. Wang, et al., Adaptive total variation based image segmentation with semi-proximal alternating minimization, *Signal Process.* 183 (2021) 108017.
- [7] L.C. Chen, G. Papandreou, I. Kokkinos, et al., Deeplab: semantic image segmentation with deep convolutional nets, atrous convolution, and fully connected CRFs, *IEEE Trans. Pattern Anal. Mach. Intell.* 40 (4) (2017) 834–848.
- [8] K. Ding, L. Xiao, G. Weng, Active contours driven by region-scalable fitting and optimized Laplacian of gaussian energy for image segmentation, *Signal Process.* 134 (2017) 224–233.
- [9] C. Le Guyader, C. Gout, Geodesic active contour under geometrical conditions: theory and 3D applications, *Numer. Algorithms* 48 (1–3) (2008) 105–133.

- [10] J. Spencer, K. Chen, A convex and selective variational model for image segmentation, *Commun. Math. Sci.* 13 (6) (2015) 1453–1472.
- [11] Y. Atiq, N. Badshah, A new model for image selective segmentation with prior information, *Sci. Int.* 28 (4) (2016) 3500–3507.
- [12] J. Zhang, K. Chen, B. Yu, et al., A local information based variational model for selective image segmentation, *Inverse Probl. Imaging* 8 (1) (2014) 293–320.
- [13] J. Spencer, K. Chen, J. Duan, Parameter-free selective segmentation with convex variational methods, *IEEE Trans. Image Process.* 28 (5) (2018) 2163–2172.
- [14] M. Roberts, K. Chen, K.L. Irion, Multigrid algorithm based on hybrid smoothers for variational and selective segmentation models, *Int. J. Comput. Math.* 96 (8) (2019) 1623–1647.
- [15] J. Song, C. Yang, L. Fan, et al., Lung lesion extraction using a toboggan based growing automatic segmentation approach, *IEEE Trans. Med. Imaging* 35 (1) (2015) 337–353.
- [16] T. Brosch, L.Y.W. Tang, Y. Yoo, et al., Deep 3D convolutional encoder networks with shortcuts for multiscale feature integration applied to multiple sclerosis lesion segmentation, *IEEE Trans. Med. Imaging* 35 (5) (2016) 1229–1239.
- [17] J. Ma, J. He, X. Yang, Learning geodesic active contours for embedding object global information in segmentation CNNs, *IEEE Trans. Med. Imaging* 40 (1) (2021) 93–104.
- [18] Y. Xie, J. Zhang, H. Lu, et al., SESV: accurate medical image segmentation by predicting and correcting errors, *IEEE Trans. Med. Imaging* 40 (1) (2021) 286–296.
- [19] Y. Ding, J. Liu, X. Xu, et al., Uncertainty-aware training of neural networks for selective medical image segmentation, *Medical Imaging Deep Learn. PMLR* (2020) 156–173.
- [20] H. Wu, J. Pan, Z. Li, et al., Automated skin lesion segmentation via an adaptive dual attention module, *IEEE Trans. Med. Imaging* 40 (1) (2021) 357–370.
- [21] M. Kass, A. Witkin, D. Terzopoulos, Snakes: active contour models, *Int. J. Comput. Vis.* 1 (4) (1988) 321–331.
- [22] V. Caselles, R. Kimmel, G. Sapiro, Geodesic active contours, *Int. J. Comput. Vis.* 22 (1) (1997) 61–79.
- [23] C. Gout, C. Le Guyader, L. Vese, Segmentation under geometrical conditions using geodesic active contours and interpolation using level set methods, *Numer. Algorithms* 39 (1–3) (2005) 155–173.
- [24] N. Badshah, K. Chen, G. Sapiro, Image selective segmentation under geometrical constraints using an active contour approach, *Commun. Comput. Phys.* 7 (4) (2010) 759–778.
- [25] T.F. Chan, L.A. Vese, Active contours without edges, *IEEE Trans. Image Process.* 10 (2) (2001) 266–277.
- [26] L. Rada, K. Chen, Improved selective segmentation model using one level-set, *J. Algorithms Comput. Technol.* 7 (4) (2013) 509–540.
- [27] H. Ali, S. Faisal, K. Chen, Image-selective segmentation model for multi-regions within the object of interest with application to medical disease, *Vis. Comput.* 6 (2020) 1–17.
- [28] L. Rada, K. Chen, A new variational model with dual level set functions for selective segmentation, *Commun. Comput. Phys.* 12 (1) (2012) 261–283.
- [29] L. Rada, H. Ali, H.N.A. Khan, A selective segmentation model for inhomogeneous images, in: *International Symposium on Intelligent Computing Systems*, Springer, Cham., 2018, pp. 123–136.
- [30] M. Roberts, K. Chen, K.L. Irion, A convex geodesic selective model for image segmentation, *J. Math. Imaging Vis.* 61 (4) (2019) 482–503.
- [31] F. Zhao, X. Xie, An overview of interactive medical image segmentation, *Ann. BMVA* 2013 (7) (2013) 1–22.
- [32] C. Liu, M.K.P. Ng, T. Zeng, Weighted variational model for selective image segmentation with application to medical images, *Pattern Recognit.* 76 (2018) 367–379.
- [33] R. Zhang, X. Feng, L. Yang, et al., Global sparse gradient guided variational Retinex model for image enhancement, *Signal Process. Image Commun.* 58 (2017) 270–281.
- [34] I. Ekeland, R. Temam, *Convex Analysis and Variational Problems*, Society for Industrial & Applied Mathematics, 1999.
- [35] S. Osher, R. Fedkiw, *Level Set Methods and Dynamic Implicit Surfaces*, Springer, Berlin, 2003.
- [36] S. Osher, J.A. Sethian, Fronts propagating with curvature-dependent speed: algorithms based on Hamilton-Jacobi formulations, *J. Comput. Phys.* 79 (1) (1988) 12–49.
- [37] H.H. Chang, A.H. Zhuang, D.J. Valentino, et al., Performance measure characterization for evaluating neuroimage segmentation algorithms, *NeuroImage* 47 (1) (2009) 122–135.
- [38] A.A. Taha, A. Hanbury, Metrics for evaluating 3D medical image segmentation: analysis, selection, and tool, *BMC Med. Imaging* 15 (1) (2015) 1–28.
- [39] X. Cai, R. Chan, T. Zeng, A two-stage image segmentation method using a convex variant of the Mumford–Shah model and thresholding, *SIAM J. Imaging Sci.* 6 (1) (2013) 368–390.
- [40] G. David, *Singular Sets of Minimizers for the Mumford–Shah Functional*, Birkhauser, 2005.